Carbon-Supported PtNi Nanocrystals for Alkaline Oxygen Reduction and Evolution Reactions: Electrochemical Activity and Durability upon Accelerated Stress Tests

Victor Shokhen, Melina Zysler, Meital Shviro, David Zitoun, Marian Chatenet

▶ **To cite this version:**

Victor Shokhen, Melina Zysler, Meital Shviro, David Zitoun, Marian Chatenet. Carbon-Supported PtNi Nanocrystals for Alkaline Oxygen Reduction and Evolution Reactions: Electrochemical Activity and Durability upon Accelerated Stress Tests. ACS Applied Energy Materials, 2020, 3 (9), pp.8858-8870. 10.1021/acsaem.0c01356 . hal-02955536

HAL Id: hal-02955536

https://hal.univ-grenoble-alpes.fr/hal-02955536

Submitted on 2 Oct 2020

HAL is a multi-disciplinary open access archive for the deposit and dissemination of scientific research documents, whether they are published or not. The documents may come from teaching and research institutions in France or abroad, or from public or private research centers.

L'archive ouverte pluridisciplinaire **HAL**, est destinée au dépôt et à la diffusion de documents scientifiques de niveau recherche, publiés ou non, émanant des établissements d'enseignement et de recherche français ou étrangers, des laboratoires publics ou privés.

Carbon-Supported PtNi Nanocrystals for Alkaline Oxygen Reduction and Evolution Reactions; Electrochemical Activity and Durability upon Accelerated Stress Tests

Victor Shokhen [1-2], Melina Zysler [2], Meital Shviro[3], David Zitoun [2], Marian Chatenet* [1]*

1- Univ. Grenoble Alpes, Univ. Savoie Mont Blanc, CNRS, Grenoble INP (Institute of Engineering Univ. Grenoble Alpes), LEPMI, 38000 Grenoble, France

2- Department of Chemistry and Bar-Ilan Institute for Technology and Advanced Materials (BINA), Bar-Ilan University, Ramat Gan 5290002, Israel

3- Institute of Electrochemical and Climate Research IEK-14, Forschungszentrum Jülich GmbH, 52425 Jülich, Germany

Abstract

PtNi is amongst the most active electrocatalyst for the oxygen reduction reaction, but its stability in operation is uncertain. Intuitively, alkaline environments lead to milder degradations than acidic ones, although carbon-supported Pt-group metal nanoparticles are particularly degraded even in dilute alkaline electrolytes. To date, PtNi catalysts durability has not been characterized for alkaline oxygen reduction and evolution reactions (ORR and OER). Herein, carbon-supported shape controlled PtNi catalysts were compared in terms of activity and durability during alkaline ORR and OER. The PtNi catalysts are shape-controlled Pt-rich alloy, Ni-rich alloy, and Pt core/Ni shell (Pt@Ni) synthesized on Vulcan XC72R carbon. Their morphology and composition were evaluated by identical-location transmission electron microscopy, X-ray photoelectron spectroscopy and X-ray diffraction pre and post accelerated stress test. Compared to Pt/C and Ni/C benchmark catalysts, the core-shell and Ni-rich alloy catalysts gave high and stable OER activities. After accelerated stress test, the catalysts show two features which are believed to play a major role in the durability: a Ni-enrichment at the nanoparticles' surface and an improved attachment of the catalyst to the carbon support.

KEYWORDS: Alkaline electrolyzer; Oxygen evolution reaction; Alkaline fuel cells; Oxygen reduction reaction; Carbon-supported catalyst; Platinum nickel octahedral; Durability; Identical-location transmission electron microscopy (IL-TEM)

1. Introduction

The last century of economic and technological development was based on fossil fuels, which has huge ecological consequences, notably in terms of climate and environmental changes. A clear footprint of this situation is the level of green-house gas emission and related global warming.[1,2] Our societies are now aware of the adverse effects of fossil energies, and, over the last decades, impressive progresses in using renewable energy sources have been reached, but these render mandatory efficient storage means. Power-to-hydrogen (water electrolyzers) and then back conversion into electricity via fuel-cells could be the solution to this problem, but this strategy is not ready for the market, yet, and still requires more research and development prior being capable to replace non-renewable energies. Alkaline fuel-cells (AFC) and alkaline water electrolyzers (AWE), as well as their anion-exchange membrane counterpart (AEM) have been under intense focus over the past years, mainly because the reactions of the oxygen electrode, both the oxygen evolution reaction (OER) and the oxygen reduction reaction (ORR), exhibit better kinetics in alkaline than in acidic environments and require less platinum group metals (PGMs) for their efficient catalysis.[3] Extensive research has been attempted to find alternative catalysts to Pt or Ir, due to the scarcity of the PGMs.[4]

One huge benefit of systems operating with alkaline electrolytes is the potential use of non-PGM catalysts such as 3d transition metals (TM), 95% of papers dealing with AEMFC use Pt-based catalysts - see Figure 10 in [D.R. Dekel, Review of cell performance in anion exchange membrane fuel cells, J. Power Sources, 375 (2018) 158.]. Indeed, compared to acidic conditions, non-PGMs do not suffer intense corrosion in alkaline media and show very promising activity. The most investigated 3d-TM are Ni, Co and Fe, the best phase of Co or Ni for OER is the oxy-hydroxide phase (III), while the fully-oxidized form (IV) demonstrates less performance [5]. The active metal hydroxide phase is not stable for long-term operation. One way to improve the stability is to combine an additional element for instance a bimetallic [6] catalysts as NiFe [7] or CoFe [8], which can provide higher stability as well as better performance, and is less element-consuming than stand-alone metal electrodes. The interest of conducting the ORR in alkaline media is rather similar; non-noble metals can be stable and active, enabling to supress or decrease the use of PGM. For example, PGM can be combined with non-precious 3d-TM such as Fe[9], Co[10], Ni[11], etc. [12–14] to form more active ORR catalysts. Famous examples of PGM combination with non-precious metal are PtNi [12,15] and PtCu [16], these materials being also popular (because very active) for acidic ORR applications [17–21]. The aforementioned 3d-TMs can also be utilized as standalone catalysts, with Cu-carbon[22] and Fe-N-C [23], showing good activity for the ORR.

On the other hand, PGM-based OER and ORR catalysts face stability issues in alkaline environments, despite the initial beliefs that “alkaline stability is superior”. It was recently found that the rate of dissolution of the metals in alkaline electrolytes is very significant in potential regions relevant to oxygen reactions.[24–26] In addition, carbon-supported Pt nanoparticles are not stable when cycled in potential in the stability domain of water, essentially because Pt assists the local corrosion of the carbon substrate, which destroys the anchoring point of the nanoparticles and leaves them un-attached to carbon, leading to pronounced nanoparticles detachment and thus of severe electrochemical surface area (ECSA) loss.[27–30] Zadick et al. demonstrated similar (although less pronounced) effects for Pd/C nanoparticles [31], and showed that shaped Pd nanoparticles were also unstable in mild alkaline degradation tests [32], being incapable to maintain their (cubic) shape upon potential cycling. Strasser et al. ended to similar conclusion for octahedral PtNi nanoparticles in acidic environments [33]. However, introducing some Ni in Pd nanoparticles was proven as an interesting strategy to enhance the durability of PdNi/C nanoparticles [34]. Of course combining a PGM with a

cheaper and more available 3d metal is popular, and it is safe to say that both shaping and combining multiple elements is able to reduce the amount of expensive and scarce PGM while hopefully increasing the activity and stability of the catalyst [35].

In this study, shaped platinum and nickel supported on carbon are prepared in different phases, as alloys or core-shell nanoparticles (NPs). The proportion of nickel was varied from Ni-rich to Pt-rich alloy. The materials were fully investigated via X-ray photoelectron spectroscopy (XPS), X-ray diffraction (XRD) and identical-location transmission electron microscopy (IL-TEM), to evaluate their structure and composition prior and after the AST and link the catalysts' activity to their structure and composition. These data enable to conclude about the possible merit of combining Ni and to achieve both high activity and stability for alkaline ORR and OER.

2. Experimental Section

2.1 Chemicals and Materials

Nickel(II) acetylacetonate ($Ni(acac)_2$, 95%) was purchased from Strem chemicals. Platinum(II) acetylacetonate ($Pt(acac)_2$, Pt 48%min), N, N-Dimethylformamide, (DMF, 99%) and benzoic acid (ACS, 99.5%) were purchased from Alfa Aesar. Benzyl alcohol (Bn 99%) was purchased from Acros Organics. Isopropanol (HPLC grade) and ethanol absolute were purchased from AR-b Bio-Lab. Vulcan XC72R carbon used as support material was purchased from Cabot Corporation. For comparison purposes, Pt/XC72 carbon (20wt%, simply denoted as Pt/C) was purchased from Johnson Matthey and used as benchmark. All materials were used as received without further purification.

2.2 Synthesis methods

Three distinctive carbon-supported octahedral Pt-Ni nanoparticles (NPs), namely Core-shell Pt@Ni, Ni-rich PtNi, and Pt-rich PtNi, were synthesized via solvothermal reaction and obtained above 90% yield.

Pt-rich Pt-Ni nanoparticles. To disperse the support in the reducing solvent, 15 mg of Vulcan XC72R carbon were added in a glass vial of 28 mL volume with 7.5 mL of a DMF:Bn mixture (4:1) (in molar ratio), and magnetically-stirred overnight. 7.5 mg of $Pt(acac)_2$, 1.6 mg of $Ni(acac)_2$, and 45.8 mg of bezoic acid were included in the vial. The mixture was sonicated for 40 min in a sonication bath. After, the vial was heated to 160°C (5°C/min) and maintained at this temperature for 12 h. To precipitate the sample, 20 mL of acetone was used. After 3 cycles of washing with ethanol and centrifugation, the sample was dried at room temperature.

Ni-rich Pt-Ni nanoparticles. Similar to the previous procedure, 30 mg of Vulcan XC72R carbon were added inside in a 28 mL-glass vial with 15 mL of DMF:Bn mixture 1:3 (in molar ratio). The suspension was magnetically-stirred overnight. 15 mg of $Pt(acac)_2$, 29.4 mg of $Ni(acac)_2$ and 91.5 mg of benzoic acid were included in the vial. After 40 min of sonication, the vial was heated to 160°C (5°C/min) and maintained at this temperature for 12 h. To precipitate the sample, 20 mL of acetone was used. After 3 cycles of washing with ethanol and centrifugation, the sample was dried at room temperature.

Pt-core Ni-shell nanoparticles (core-shell PtNi). 80 mg of Vulcan XC72R carbon was dispersed into 40 mL of DMF and stirred overnight inside a sealed glass bottle (Duran®). 80 mg of $Pt(acac)_2$, and 45.8 mg of benzoic acid were added. The mixture was sonicated for 40 min. The resulting suspension of Pt/C was heated at 160°C for 12 h (5°C/min heating rate) under gentle magnetic stirring, cooled down to

room temperature, washed and precipitated several times using acetone and ethanol (at least twice each of the solvent or until the supernatant is transparent), and then dried at room temperature. In a second step, the Ni shell was prepared: 10 mL of DMF and 20 mL of benzyl alcohol were put into a glass sealed bottle and sonicated for 15 min. 60 mg of Pt/C were dispersed in the solvent mixture and stirred overnight. 29.4 mg of $Ni(acac)_2$ and 91.5 mg benzoic acid were incorporated into the dispersion and sonicated for 40 min. After 12 h heating at 160°C (5°C/min heating rate), the sample was washed and centrifugated using ethanol, and acetone, and then dried at room temperature.

Ni/C synthesis: Carbon black (Vulcan XC72R, 200 mg) was dispersed in mesitylene (100 mL) under vigorous stirring. In a glovebox, $Ni(COD)_2$ (190 mg, 0.69 mmol) was dissolved in 40 mL dry Toluene. The yellow solution was added to the Vulcan XC72R suspension. The mixture was heated to 110°C under stirring for 1 h under N_2 atmosphere. The resulting NPs were precipitated by centrifugation (11,000 rpm x 20 min) and washed 3 times with a mixture of ethanol:toluene (1:1) (11,000 revolution per min (rpm) x 15 min) and then with ethanol (11,000 rpm x 15 min). The NPs were dried at 70°C for 24 h and finally at 150°C for 4 h, under high vacuum in order to remove residues of organic materials.

2.2 Electrochemistry

A glassy-carbon rotating disk electrode (RDE) tip was polished until mirror-finish with diamond suspensions of 1 µm and then 0.1 µm, sonicated in acetone, isopropanol and then water for 15 min for each solvent, prior drying in an oven in 120°C. Then, thin-film RDE was prepared by depositing inks of the relevant catalyst. The 2 $mg_{catalyst}$ mL^{-1} ink contained 80% isopropanol and 20% MQ-grade water (18.2 MΩ cm, < 3 ppb total organic carbon, Elix +Milli-Q Element, Millipore) and 1% Nafion solution. The ink was sonicated for 45 min until homogenous (without visible aggregates). An active layer loaded at 10 µg cm^{-2} of catalyst was deposited on a clean 5 mm diameter glassy-carbon RDE while rotating at 600 rpm; the ink was dried with a heat-blower for 20 min while the RDE was rotated, leading to a uniform black matt texture (as described in the study of Garsany et al. [36]).

All electrochemistry measurements were performed in a three-electrode cell using a VMP-3 potentiostat (Bio-Logic). 1 M KOH (Alfa Aesar, KOH Pellets, 99.98%) electrolyte solution with MQ-grade water was used in all electrochemical measurements. The electrochemical cell was fit for the alkaline condition using a Teflon cup in the removable Pyrex cell bottom, to avoid any contact of the alkaline solution with glass, which would have adverse effects [37,38]. All experiments were performed at 25°C under Ar(g) (99.999%) for oxygen evolution reaction and supporting electrolyte cyclic voltammetry, and Oxygen(g) (99.999) for oxygen reduction, in all case at atmospheric pressure (1 atm). A platinum mesh was used as the counter-electrode. The reference electrode was a freshly-prepared reversible hydrogen electrode (RHE), and a new RHE was made every 2-3 hours to avoid any shift or bias in the potential reference value. The rotating disk electrode was used as working electrode with a rotating rate of 1,600 rpm to avoid catalyst blockage from gas bubbles. All the measurements were corrected for iR loss in a dynamic manner (ZIR correction). Before each experiment, the electrolyte was purged for 20 min with the relevant gas. The cyclic voltammetry (in supporting electrolyte) were measured at a potential scan rate of 100 mV s^{-1} under Ar in the stability domain of water; OER CVs were measured in the potential range 1.2 – 1.6 V *vs* RHE at a scan rate of 5 mV s^{-1}, also under Ar purge; ORR measurement were done from 0.05 to 1.05 V *vs* RHE at a scan rate of 10 mV s^{-1} under oxygen atmosphere. Accelerated stress tests (AST) were also conducted as "ORR load cycles" or "OER load cycles". ORR load cycles consisted of 1000 steps of 3 s at 0.6 and 1.0 V *vs* RHE in oxygen-

purged electrolyte atmosphere. OER load cycles consisted of 1000 steps of 3 s at 1.2 and 1.6 V *vs* RHE in Argon-purged electrolyte. These AST were conducted on glassy-carbon RDE and also on gold transmission electron microscopy (TEM) grids (see details below) in the so-called Identical-location transmission electron microscopy (IL-TEM) procedure [39].

The TEM observations were done with Jeol 2010 TEM equipped with LaB_6 filament. The micrographs were taken in selected representative region at different stages of the catalysts lifetime (prior electrochemistry: new, and after the ORR and OER accelerated stress-tests) to highlight the potential changes of the catalyst materials after AST and to link these changes to the on-time-measured activity.

The ILTEM measurements were done by using gold grids (Lacey-carbon TEM gold grid 300 mesh) as the catalyst support, gold being chosen as TEM grid material to avoid side catalytic effect and detrimental corrosion which could poison the catalyst. The grids were prepared with the inks described above. The electrochemical procedures to test the ILTEM grids as working electrode were the same than for RDE tests. Particle size distribution (PSD) histograms were constructed by counting the nanoparticles in similar regions before and after the ASTs, and to probe differential size change. Besides PSD, a qualitative comparison of the nanoparticles' shape and particle detachment was also done to highlight the proportion of structure change from octahedral to spherical structure and the particle detachment.

High-resolution TEM images (HRTEM) and the high-angle annular dark-field scanning transmission electron microscope (HAADF-STEM)-energy-dispersive X-ray spectroscopy (EDS) were taken on a FEI TITAN transmission electron microscope operated at 300 kV. STEM-EDS elemental mapping was performed using FEI Titan 80-200 electron microscope equipped with a C_S -probe corrector (CEOS GmbH) and a HAADF detector. "Z-contrast" conditions were achieved by using a probe semi-angle of 25 mrad and an inner collection angle of the detector of 75 mrad.

X-ray diffraction (XRD) diagrams were acquired in acquisition-reflexion mode in the Bragg Brentano geometry, using a X'Pert Pro MPD by PANalytical device, equipped with a copper anode and operated with the K_{alpha} wavelength of Cu (0.15419 nm).

X-ray photoelectron spectra (XPS) were obtained using a Thermo Scientific K-alpha spectrometer with a monochromated Al X-ray source (hν =1486.6 eV; spot size 400 µm). The survey spectra and core level record was used with pass energies of 100 and 30 eV, respectively. All spectra were acquired using an electron flood-gun to compensate possible positive charge accumulation during the measurements. The obtained spectra were analysed with the Thermo Scientific Advantage Software.

3. Results and discussion

3.1 Initial physical and electrochemical characterization of the PtNi catalysts

Three types of shape-controlled Pt-Ni nanoparticles were synthesized on Vulcan XC72R carbon via colloidal syntheses from metal acetylacetonate complexes: Pt-rich and Ni-rich alloys through a one-pot reaction and core-shell Pt@Ni following a two-step reaction (Pt seeds followed by Ni growth) explained in details in the experimental section. We compared the catalytic properties to Ni/C and Pt/C. Since $Ni(acac)_2$ alone does not react with dimethylformamide [40], and the growth of Ni is

observed only in the presence of Pt seeds, Ni/C was synthesized from an organometallic precursor following an already published route [41], and Pt/C was obtained from a commercial source.

The purpose of the study is to investigate: (i) the contribution of each element, Pt and Ni, to the electrocatalytic effect; (ii) the significance of one-phase alloyed pre-catalyst (Ni or Pt rich) compared to a two-phase pre-catalyst (Pt core/Ni shell). The term pre-catalyst relates to the materials before any electrocatalysis. The pre-catalysts were submitted to two types of accelerated stressed tests (AST). In the following, the pristine pre-catalyst and the catalysts after AST have been characterized by XRD, XRF, TEM (with identical location) and XPS.

The X-ray diffractograms of the pre-catalysts correspond to the face-centered cubic (FCC) crystalline structure in all of the synthesized NPs (Figure 1). The peak broadening is due to the small size of the NPs. The crystallographic features of the Vulcan XC72R carbon support appear at lower angles and are not shown here. The Pt-rich pre-catalyst shows asymmetric broad peaks of the {111} and {200} lattice planes of Pt, with a small shoulder at larger Bragg angles as a result of Ni alloying. Ni-rich pre-catalysts shows a dominant asymmetric peak close to the {111} lattice plane of Ni, and a broad shoulder close to the {111} lattice plane of Pt. In both cases, for Pt-rich and Ni-rich NPs, the XRD is consistent with a Pt-rich and a Ni-rich alloy respectively, with a composition gradient. Core-shell PtNi NPs show two distinct phases, which can be attributed to the concomitance of Pt-rich and Ni-rich phases. The Ni-rich phase displays narrower peaks, signing the presence of larger crystallites than the Pt-rich seeds.

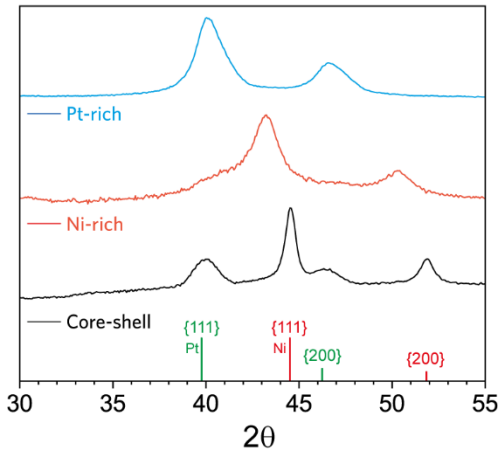

Figure 1. *XRD diagram of the three PtNi NPs types; Core-shell Pt@Ni (black), Ni-rich PtNi (red), and Pt-rich PtNi(blue).*

X-ray fluorescence (XRF) spectroscopy (Figure S1 in supporting information) shows an average elemental ratio of $PtNi_{11}$ (Core-shell), $PtNi_6$ (Ni-rich) and $Pt_{3.5}Ni$ (Pt-rich).

Low-resolution TEM characterization are displayed in Figure 2. The observed nanoparticles are predominantly of octahedral shape (> 90%) and distributed on the carbon support. One nevertheless sees that the nanoparticles distribution is more homogeneous for the Pt-rich sample (isolated NPs covering the whole carbon surface), larger agglomerates and uncovered carbon regions being witnessed for the Ni-rich and core-shell catalysts. High-resolution X-EDS elemental maps were obtained in STEM mode for representative octahedral NPs of each type; Pt is marked in red and Ni in green. The core-shell nanoparticles display a clear segregation between the Pt core and the Ni shell;

the latter covers the Pt core. The Ni-rich NPs show a well-defined octahedral shape, with a Pt segregation on the edges of the particle. Pt-rich NPs essentially display a homogeneous composition.

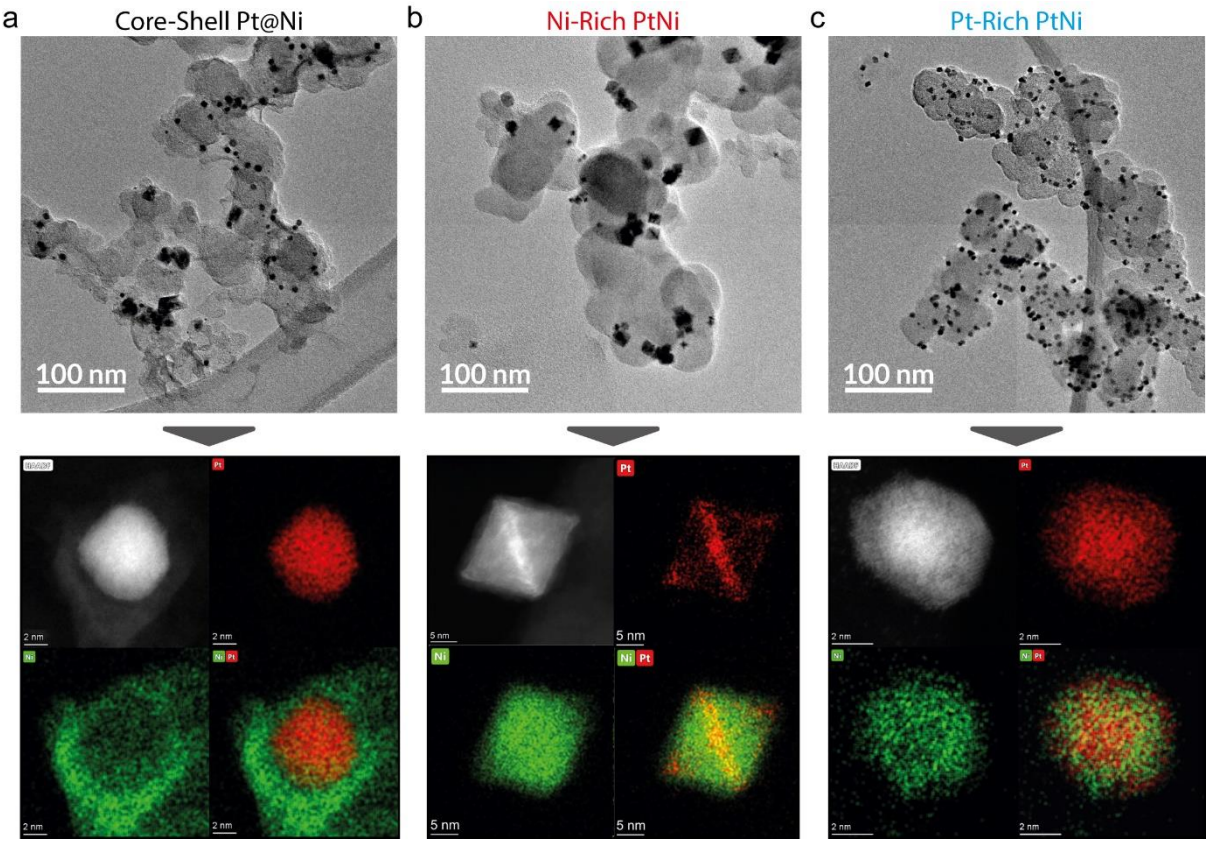

Figure 2. Representative low-resolution TEM micrographs of the samples, and corresponding high-resolution STEM-HAADF images and XEDS mapping of representative NPs; Core-Shell Pt@Ni (a), Ni-rich PtNi (b), Pt-rich PtNi (c),

Figure S2 shows the particle size distribution of the three samples; the core-shell NPs have a mean size of 6.8 ± 1.3 nm with a small percentage of extraordinary (very large) particles size, while the Ni-rich displays a larger mean size and broader size distribution (mean size of 14.8 ± 5.2 nm), and the Pt-rich exhibits a narrow size distribution with a mean-size of 6.3 ± 1.4 nm.

These pre-catalysts PtNi/C display the features needed for an in-depth comparison of their electrochemical properties. The cyclic voltamperograms of the PtNi/C catalysts were collected on a glassy carbon rotating disc electrode in the electrochemical window 0.05 < *E* < 1.2 V *vs* RHE (Figure 3a). Commercial Pt/C and synthesized Ni/C were measured for comparison. All the measurements are conducted at 298 K in a 1 M KOH electrolyte and a glass-free electrochemical set-up.

The core-shell and Ni-rich catalysts show a feature-less voltamperogram similar to Ni/C, suggesting that very little Pt sites are present at the surface of these samples. On the contrary, the Pt-rich sample exhibits similar features of hydrogen adsorption/desorption and oxide formation/reduction as Pt/C, although in a lesser extent. From these voltamperograms, the Pt electrochemical active surface area (ECSA) area can be estimated, based on the region of hydrogen adsorption/desorption (0.05 < *E* < 0.5 V *vs* RHE). Pt-rich and Pt/C catalysts exhibit the largest *Pt ECSA*. Additional voltamperograms were collected in the region of the nickel redox activity (Ni^{2+}/Ni^{3+}), for 1.25 < *E* < 1.45 V *vs* RHE (Figure 3b).

All the Ni-containing samples (and not Pt/C, but this was naturally expected) show a nickel redox (Ni^{2+}/Ni^{3+}) activity, and the *nickel ECSA* can be determined by integration of the corresponding peaks. The presence of this redox transition reveals the spontaneous formation of oxidized nickel species on the surface of the NPs in alkaline electrolyte. Interestingly, the nickel redox couple potential depends on the presence of platinum, with a shift to lower potential in the presence of Pt. Although it is challenging to provide accurate data on *Ni ECSA* compared to the well-established *Pt ECSA*, these data can give a rough estimate of the catalytic area (Table 1). The Core-shell catalyst displays a total ECSA exceeding the geometric surface as observed by TEM. This result exposes the limitations of defining the ECSA by the redox activity of the Ni(II)/Ni(III) species. In this case, the redox activity relates not only to the surface species but to also the underneath Ni layers. In the following, we shall consider the relative variations of the ECSA with the accelerated stress tests.

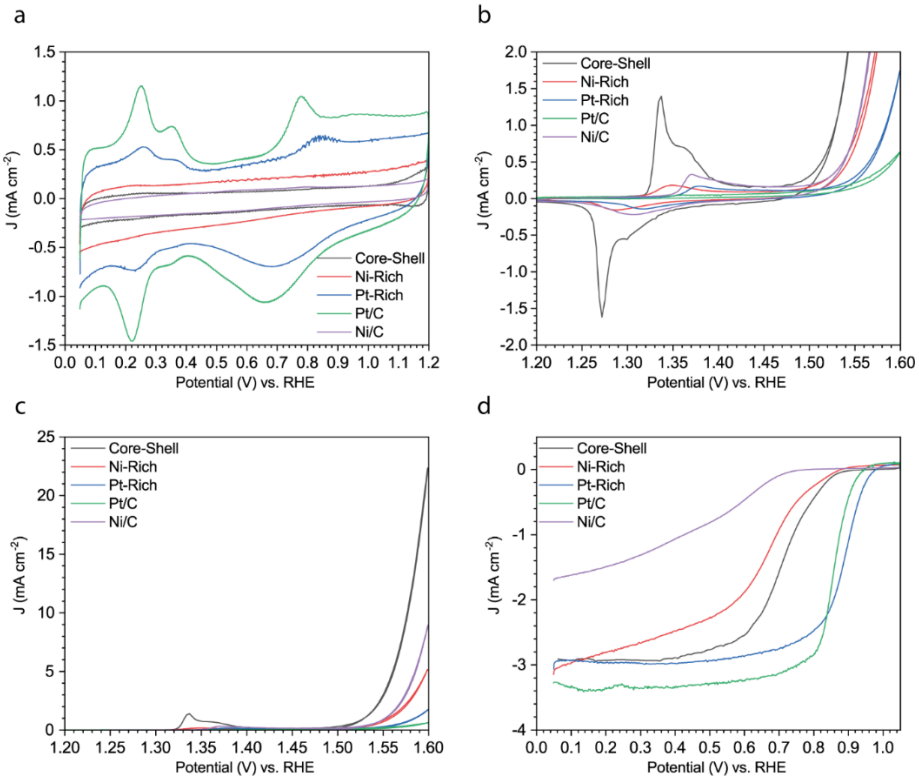

Figure 3. *Initial voltamperograms of the catalysts measured in 1 M KOH, 298 K at 100 mV s^{-1} (a). Corresponding nickel redox area (Ni^{2+}/Ni^{3+}) scanned at 5 mV s^{-1} (b). Oxygen evolution reaction on the various catalysts, measured at 5 mV s^{-1} and 1600 rpm (c). Oxygen reduction reaction on the various catalysts, measured at 10 mV s^{-1} and 1600 rpm (d).*

The initial OER activity of the catalyst is presented in Figure 3c. Although Pt is a reliable benchmark catalyst for many reactions, it shows very little OER activity (up to 1.6 V); indeed, at that stage, Pt surface is oxidized [42] and exhibits both poor conductivity and OER catalytic activity. On the contrary, Ni/C displays a better OER activity with a low-potential OER onset (activity of 1 mA cm^{-2} at 1.552 V *vs* RHE and 8.8 mA cm^{-2} at 1.6 V *vs* RHE). Combining Ni with Pt improves the OER activity: the Ni-rich and Pt-rich catalysts show larger OER activity than Pt/C, while the Core-shell Pt@Ni shows great initial OER activity (1 mA cm^{-2} measured at 1.528 V *vs* RHE and 10 mA cm^{-2} at 1.575 V *vs* RHE), even better than Ni/C.

In summary, Ni-rich catalysts are much better OER catalysts than Pt-rich catalysts. The presence of Pt, whether in the shell or in the core of the bimetallic catalysts, enhances the catalytic activity of Ni. It is too early to determine the exact catalytic sites of the bimetallic catalysts but it seems obvious that the combination of a high content of Ni and small amount of Pt, preferentially in the core, shows the best activity for the OER.

The initial ORR activity was measured in the potential window of 0.05 < *E* < 1.05 V *vs* RHE (Figure 3d). For this reaction, Pt is usually considered as a benchmark; the commercial Pt/C shows a good initial ORR activity (-0.44 mA cm^{-2} at 0.9 V *vs* RHE) while the Pt-rich catalyst provides a twice higher activity (-1.1 mA cm^{-2} at the same potential). The higher activity of the Pt-rich sample results from its alloying with Ni, that reduces the adsorption strength of adsorbed oxygen intermediates, thereby improving the ORR kinetics (the well-known electronic effects) [43–45]. The Core-shell and Ni-rich samples exhibit lower ORR onset potentials, their Ni-rich surfaces failing to trigger fast ORR at high potential: -1 mA cm^{-2} is only measured at 0.74 and 0.69 V *vs* RHE, respectively.

Table 1: Pt and Ni ESCA of the three PtNi electrocatalysis. Activity markers of OER (Current density measured at potential 1.6 *vs* RHE) and ORR (half-wave potential, measured on a RDE plot at 1,600 rpm, *vs* RHE)

Sample	***Pt ECSA*** H_{upd} **(cm^2)**	***Ni ESCA*** $Ni^{II}Ni^{III}$ **redox (cm^2)**	**Total active area (cm^2)**	***j* at 1.6 V *vs* RHE OER (mA $cm^{-2}_{geometric}$)**	$E_{1/2}$ **ORR (V *vs* RHE)**
Core-Shell Pt@Ni	Negligible	31.2	31.2	22.4	0.705
Ni-Rich PtNi	Negligible	5.56	5.56	5.2	0.690
Pt-Rich PtNi	3.50	4.76	8.26	1.7	0.885

3.2. Aging process of the PtNi catalysts through accelerated stress test.

After the initial ORR characterization, a second OER characterization was performed and all the catalysts that contain Ni exhibited improved OER electrocatalysis performance at that stage (Figure 4a): the purple dashed-line plot shows the improved OER activity after the initial ORR (and before any AST). More specifically, the Core-shell catalyst shows spectacular improvement of its OER activity, reaching 10 mA cm^{-2} at 1.545 V *vs* RHE, an improvement of 30 mV versus its initial state, and 79 mA cm^{-2} at 1.6 V *vs* RHE. The Ni-rich sample also shows a significant improvement, reaching 10 mA cm^{-2} at 1.56 V *vs* RHE, a shift of 35 mV, and 68 mA cm^{-2} at 1.6 V *vs* RHE. The Ni/C benchmark catalyst exhibits improved OER activity, 10 mA cm^{-2} being obtained at 1.567 V *vs* RHE and 41 mA cm^{-2} being measured at 1.6 V *vs* RHE (Figure S3). On the contrary, the Pt-rich samples only demonstrate a minor increase in OER compared to the initial OER (Pt-rich PtNi) or no improvement at all (Pt/C). This improvement of OER activity of the Ni-rich samples may be connected to the building of proper Ni-oxides, which are

known to be very active for the alkaline OER [46,47]. This change of surface structure will be further explored after the ORR or OER accelerated stress tests (AST).

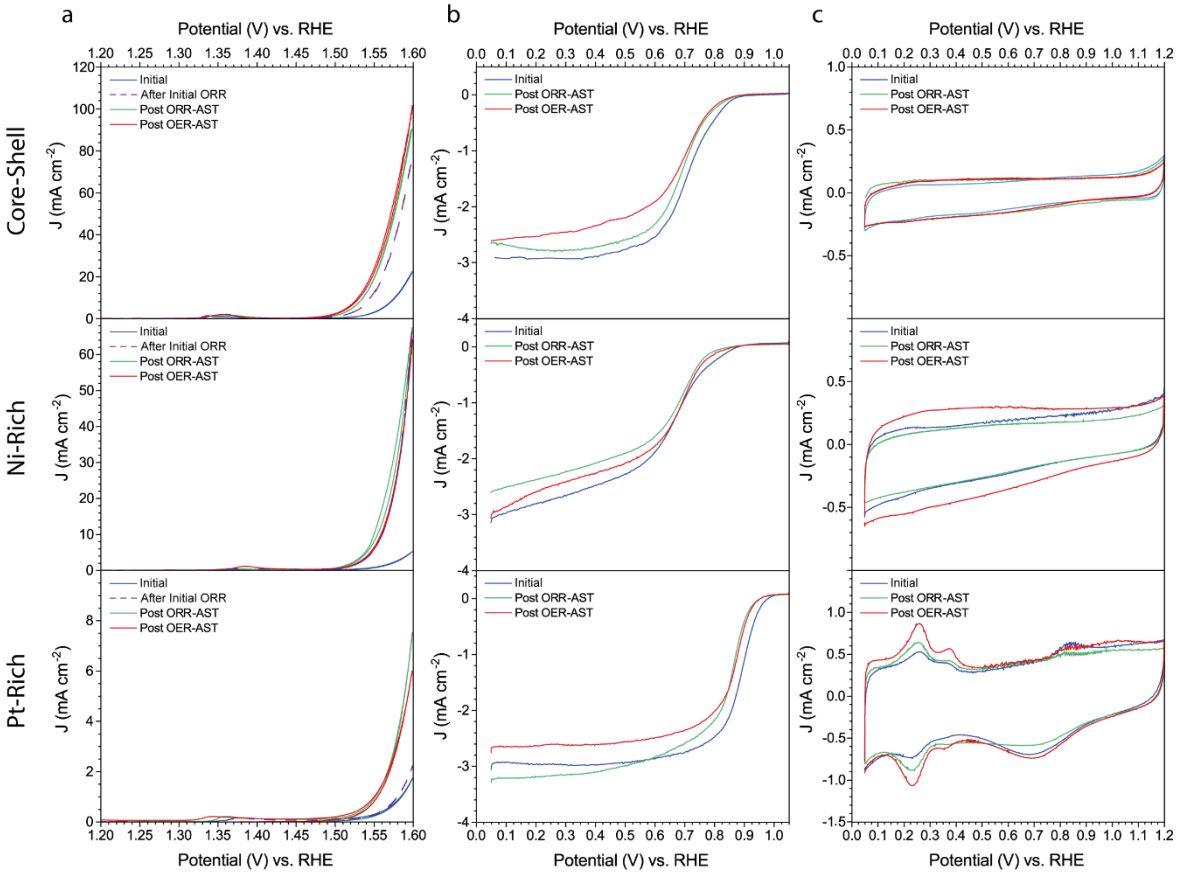

Figure 4. *OER (a) and ORR (b) voltamperograms monitored prior/after accelerated stress tests for the Core-shell (top), Ni-rich (middle) and Pt-rich (bottom) catalysts. The initial curves are based on the fresh voltamperograms. Evolution of the CV behaviour of the catalysts in supporting electrolyte prior/after operation (c).*

To further investigate this phenomenon, the samples were submitted to accelerated stress test consisting of "ORR cycling" (1000 steps of 3 s each at 0.6 and 1 V *vs* RHE) or "OER cycling" (1000 steps of 3 s each at 1.2 and 1.6 V *vs* RHE).

For the three PtNi samples, the OER activity markedly increases after both AST procedures, very little differences being noticed between the post-ORR-AST and post-OER-AST tests. The Core-shell catalyst (Figure 4a), which was the best OER catalyst after the ORR characterization, shows a small improvement of its OER activity after the two AST procedures (Table 2): 10 mA cm^{-2} is recorded at 1.535 V post-ORR and 1.530 V OER AST, respectively, an additional decrease of 10 and 15 mV compared to its performances post-ORR characterization. At that stage, the current at 1.6 V *vs* RHE reaches 90 and 102 mA cm^{-2} post-ORR and OER AST, respectively. After the OER-AST, the Ni-rich catalysts shows 1/3 lower activity than the Core-shell (64 mA cm^{-2} recorded at 1.6 V *vs* RHE), and it is only marginally improved after the ORR-AST. Finally, although the Pt-rich catalyst also exhibits an improved OER activity after the two ASTs, its performances remain very modest: the activity does not reach 10 mA cm^{-2} up to 1.6 V *vs* RHE. This is in line with the behaviour of Pt/C (Figure S3), which remains by far the worst catalyst and almost stays the same after the ASTs. Finally, Ni/C shows stable OER activity after the ORR-AST but lower activity after OER-AST, probably as a result of uncontrolled

Ni-oxide formation. As such, it seems that the presence of Pt core or Pt edges has a very beneficial impact on the OER activity of the Ni rich samples. Table 2 presents a summary of the results.

Figure 4b show the results of ORR characterizations post ASTs. For the Core-shell catalyst, the ORR onset decreased after both ASTs, and the reaction kinetics is non-negligibly depreciated (the half-wave potential is shifted negative); besides, the limiting current density also decreases in absolute value, all these changes signing that the aged Core-shell catalyst has depreciated ORR performances; these changes are more pronounced after the OER-AST. For the Ni-rich and Pt-rich samples, a similar trend is noted, although the initial advantage of the Pt-rich sample over the two other catalyst still maintains after the ASTs. Concerning Ni/C (Figure S3), it shows almost no ORR activity post AST (the same as in its initial state). For Pt/C, the decay in ORR activity post AST is very spectacular; it is more pronounced post-ORR-AST than post-OER-AST, which is not intuitive; at that stage, one could incriminate (i) the more pronounced Pt dissolution and Ostwald ripening and (ii) the Pt-assisted carbon-corrosion, when Pt is not passivated and repeatedly-cycled below/above the onset of Pt-oxides formation (ORR-AST), whereas when Pt is always oxidized (OER-AST) the two types of phenomena are severely hindered[48–52].

The voltamperograms in figure 4c provide further insights into the physicochemical changes undergone by the tested catalysts. Whereas the changes for the Core-shell catalyst are minimal, whatever the AST considered (the Ni/C benchmark also shows no change in the CV pre/post-AST on the supporting CV, Figure S3), both the Ni-rich and Pt-rich exhibit marked differences after compared to prior the ASTs. For Ni-rich, the double layer current slightly decreases post-ORR-AST and strongly increases post-OER-AST; this denotes for intense carbon functionalization in the latter case (which is the preliminary step of carbon corrosion). In addition, even though the Pt features (H-upd peaks for $0 < E < 0.4$ V *vs* RHE) are slight in the pristine Ni-rich sample, they are completely absent in the aged samples, either because of preferential dissolution of the Pt (unlikely), or because Ni leaches out and subsequently covers the surface Pt atoms. This scenario will be studied in more details below. For the Pt-rich catalyst, the trend is exactly opposite: the Pt features (both the H-upd peaks and the Pt-oxide region: PtOx formation for $E > 0.8$ V *vs* RHE in the positive scan, and PtOx reduction in the range $0.9 > E > 0.5$ V *vs* RHE in the negative scan) are growing after ORR-AST and even more after the OER-AST. This increase in Pt behaviour evidently signs that more Pt atoms become exposed to the surface of the aged Pt-rich sample. Surprisingly, the Pt/C benchmark shows a large decrease in the Pt features (Figure S3) that may results from detachment of particles from the carbon support, evidencing that the presence of Ni positively affects the durability of the Pt-rich sample in these conditions, which will be further described below, based on the IL-TEM and XPS data.

Table 2: Activity markers of OER (potential measured at 10 mA cm^{-2} OER current density, and current density mA cm^{-2} at 1.6 V *vs* RHE) and ORR (half-wave potential), measured in RDE at 1,600 rpm

Sample	Post AST type	***J* at 1.6 V *vs* RHE OER ($mA\ cm^{-2}$)**	***E* at 10 mA cm^{-2} OER (V *vs* RHE)**	**$E_{1/2}$ ORR (V *vs* RHE)**
Core-Shell Pt@Ni	OER	102	1.530	0.692
	ORR	90	1.535	0.650
Ni-Rich PtNi	OER	64	1.560	0.695

	ORR	66	1.554	0.687
Pt-Rich PtNi	OER	6.0	1.6 <	0.865
	ORR	7.53	1.6 <	0.860

Figure S4 shows the fate of nickel redox activity (Ni^{II}/Ni^{III} transition, in the potential range $1.2 < E < 1.45$ V *vs* RHE) prior/after the ASTs. For the Ni/C catalyst, the redox waves increase with ASTs, demonstrating the larger Ni surface exposed to the electrolyte. The catalysts rich in nickel (Core-shell, Ni-rich, Ni/C) also show a noticeable increase in the nickel redox peaks, revealing a larger proportion of surface Ni^{II}/Ni^{III} after AST. In the Ni-rich samples, the peaks are shifted to higher potential after AST, closer to the ones of Ni/C, showing a larger segregation between Pt and Ni after electrochemical cycling. For the Pt-rich sample, the same trend is observed, as these redox transitions are shifted towards the potential of Ni/C catalyst. In all cases, the electrochemical cycling tends to the segregation of Pt and Ni.

There could be a correlation between catalytic activity and the redox potential value of the catalyst: it seems that the more active catalysts - core-shell, Ni-rich and Ni - show a similar oxidation point in the range of $1.34 < E < 1.36$ V *vs* RHE.

However, the oxidation Ni peak of pristine core-shell show two types of peaks: one at 1.34 V *vs* RHE that is similar to the single peak of pristine Ni/C, and the second and wider peak has a common peak location as the pristine Ni-rich at 1.36 V *vs* RHE. These two peaks of Ni oxidation may be related to Ni and several areas in the shell that is alloyed with Pt. However, there is no direct correlation between the peaks post AST and requires a more in-depth investigation.

First, the Pt/Ni ratio was checked post ASTs and the Ni content has decreased in all cases, as seen in Table 3. However, this analysis provides a total average and does not represent each particle.

Table 3. Ratio of the elements pre and post accelerated stress test (EDS).

Sample	Initial state	Post ORR-AST	Post OER-AST
Core-Shell Pt@Ni	$PtNi_{11}$	$PtNi_{4.51}$	$PtNi_{6.63}$
Ni-Rich PtNi	$PtNi_6$	$PtNi_{2.15}$	$PtNi_{1.98}$
Pt-Rich PtNi	$Pt_{3.5}Ni$	Pt_5Ni	$Pt_{11}Ni$

Identical-location (IL) TEM technique was used to observe the fate of the PtNi catalysts pre and post AST (Figure 5), and for the Pt/C and Ni/C benchmarks (Figure S5). What is very evident from Figure 5 is that none of the octahedral PtNi samples exhibit intense detachment of the particles from the carbon support, even though the fraction of detached particles starts to be detectable post OER-AST. In addition, the Pt-rich catalyst shows the highest percentage of nanoparticles lost among the PtNi samples. In comparison, the commercial Pt/C catalyst shows a significant amount of Pt NPs detachment, in agreement with previous findings from Zadick et al. and Lafforgue et al. [27,29,53] Interestingly, the potential interval of the AST matters a lot in terms of particles detachment for the catalysts with high-Pt-content (Pt-rich PtNi and Pt/C): post ORR-AST, the Pt-rich loses 51% of its initial NPs, while this value is divided by a factor *ca*. 2 post OER AST (24% NPs loss) (Figure S6a). Here again, it seems that what is detrimental to the stability of Pt-rich NPs supported on carbon is to cycle them

in potential below/above the region of Pt-oxides, in agreement with the findings derived from electrochemistry (see above) and from Zadick et al. and Lafforgue et al. [27,29,53]. On the contrary, when Pt is present in its oxidized state (as in the OER-AST), it cannot assist any carbon corrosion, and hence the Pt NPs detachment is minor; it is of course not zero, because in that potential interval, carbon is subjected to "homogeneous corrosion". For the catalysts with high initial Ni-content (Core-shell, Ni-rich and Ni/C), the degradations are obviously smaller: there is almost no visual particle loses, because there is very little surface Pt atoms to assist carbon corrosion. This does not mean that nothing happens to these materials. Indeed, for all post OER-AST micrographs, degradation of the carbon and related changes in its morphology are detected. This leads to some disconnection between carbon grains for the Core-shell post-OER (Figure 5a), because of carbon corrosion/Nafion degradation. Naturally, such carbon "homogeneous corrosion" destabilizes the supported NPs, and detectable particles drift across the carbon is monitored post ASTs for all the PtNi samples (Figure 5). Finally, the Ni/C benchmark seems very stable in the two conditions explored; this goes in line with the conclusions of Zadick et al. for Ni_3M/C catalysts [54]: Ni NPs do not favour local carbon corrosion and hence are rather stable versus NPs detachment from the carbon support.

Besides the particle detachment, the ASTs have an effect on the shape and size of the particles (Figure 5 and Figure S7). Pt-rich NPs exhibit a clear shape-change (Figure 5c) from octahedral to a spherical shape, mostly post ORR-AST. The Core-shell NPs undergo a smaller amount of particle change in terms of shape, but this mostly occurs post OER-AST. Lastly, the Ni-rich sample shows a very minor to no change in NPs shape. However, in the two last cases, there are "filaments" that develop, which are likely due to Ni-oxides formation after the ASTs. Besides, nearly all the particles witnessed non-negligible decrease in size after the ASTs (Figure S7), signing metal dissolution or exsolution. In the particular case of the Ni-rich and Core-shell catalysts, some particles show slight increase in size post OER-AST, which may be associated to the dissolution of nickel from the NPs surface followed by redeposition as Ni-oxides (Figure 5 and Figure S7).

In any case, the morphological degradations/alterations of the octahedral PtNi particles are much smaller than those experienced by the Pt/C benchmark. In addition, these small morphologic changes are combined with pronounced ORR/OER activity changes for these electrocatalysts, which must be related to their surface chemistry. For this reason, XRD and XPS analyses have been performed prior/after the ASTs (Figure 6 and Figure 7, respectively).

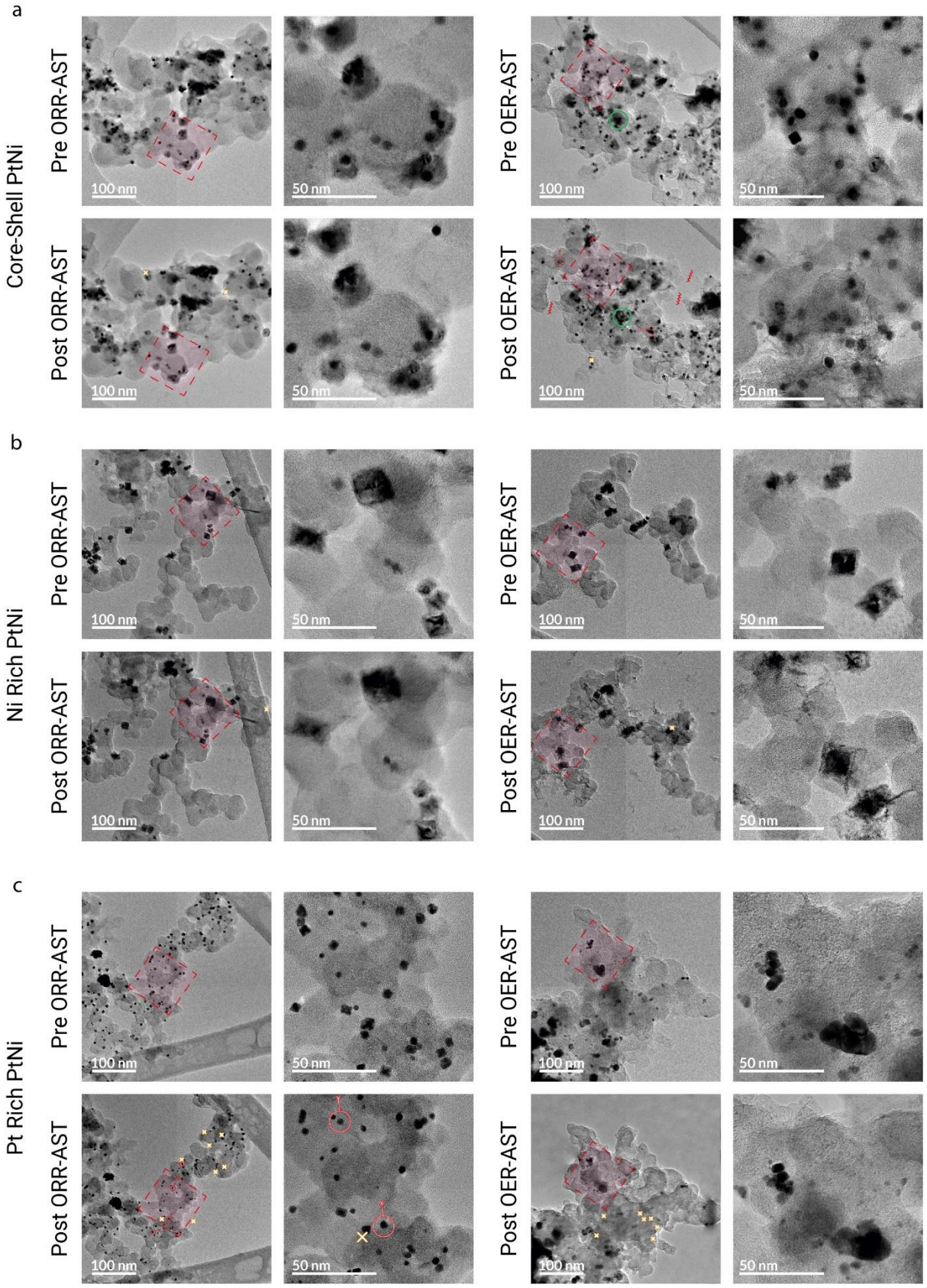

Figure 5. *Identical location transmission electron micrographs (IL-TEM) of the PtNi samples of pre and post ORR-AST (Left) or OER-AST (Right). PtNi (Pt@Ni) Core-shell (a), PtNi alloy Ni-rich (b), PtNi*

alloy Pt-rich (c). Orange-white ''X'' correspond to missing particles post-AST (this marker not being comprehensive). The red circle defines a particle '' drift''.

Comparing the XRD diagrams of the aged samples with the corresponding initial ones (Figure 6) shows the potential crystalline changes of the PtNi samples. The Pt-rich catalyst does show very minimal changes (if any), revealing that the crystalline structure of this material has hardly been affected by the ASTs. On the contrary, the Ni-rich catalyst, witnessed a clear separation of the PtNi initial alloy to more separated individual elements (Ni and Pt); in the process, the reflection peaks moved closer to their pure metal location, even though a wider variety of alloy compositions has formed broader peaks and are detected mostly post OER-AST. Overall, this confirms the results of ILTEM and electrochemistry: Ni has a tendency to segregate on the surface of the catalyst and forms a Ni metal phase.

Finally, the Core-shell catalyst shows almost no change in the crystal structure post AST, the only change noticed being the presence of a strong signal of potassium carbonate post OER-AST, signing intense carbon corrosion in that case from higher catalytic activity (in agreement with the ILTEM micrographs of Figure 5).

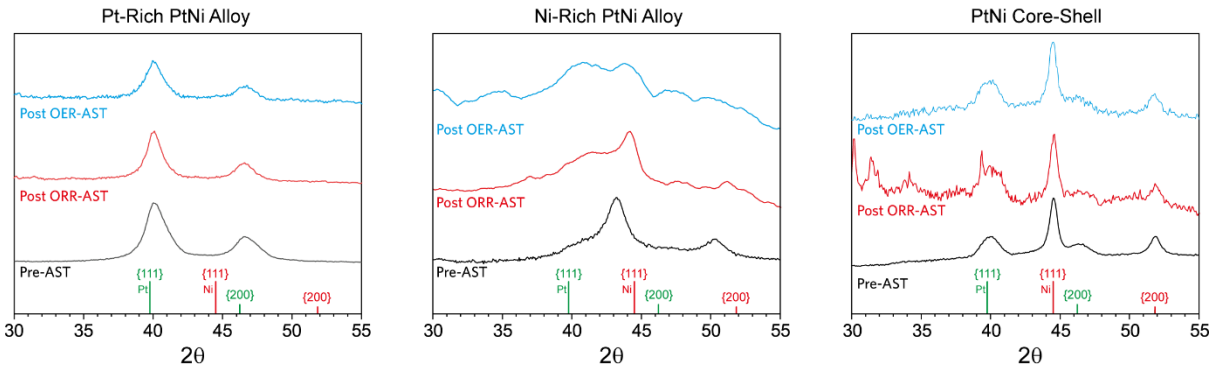

Figure 6. *Evolution of the XRD diagrams of the PtNi post-OER/ORR AST compared to the initial one (see Figure 1).*

The surface of the particles was analysed by XPS (Figure 7). Nickel oxidation state can be monitored from the Ni 2p region. Two main oxidation states of nickel are observed, Ni(0) at 852.6 eV assigned to Ni metal and Ni(II) at 856.0 eV corresponding to an hydroxide. The XPS shows an additional small shoulder of Ni(II) (NiO) at 854 eV, the signal above 858 eV corresponds to satellites of Ni oxides. Ni in Ni-rich samples can be also noticed by an additional peak at 68.0 eV (evident for the pristine Ni-rich and Core-shell samples) close to the Pt 4f region. The Pt 4f region shows Pt(0) at 71 eV and a left shoulder of PtO for stronger binding energy at 72.4 eV.

The O 1s region shows a wide peak which can correspond to a variety of oxides with a high oxygen content noticed for the core-shell sample (Figure S8). C 1s region shows similar spectrum in all initial cases (Figure S8). Additionally, at slightly higher binding energy than C 1s, K 2p shows up at 293 eV and signals the formation of K_2CO_3. In alkaline medium, the corrosion of carbon yields carbonate as a side reaction catalysed by Pt on the carbon support. This issue is particularly acute on post OER AST and Pt rich samples, which is consistent with the IL-TEM observations.

Post-AST XPS show the evolution of the electrocatalysts. Pt binding energy is practically unchanged upon cycling, except for an additional peak of PtO_2 in Ni-rich post OER-AST. In the Ni 2p region, Ni(0) peak has faded and only Ni(II) can be observed as a result of the formation of a $Ni(OH)_2$ surface layer. Correspondingly, O 1s shows an increase in the intensity post AST emphasis after OER-AST (Figure S8).

Core-shell NPs present also a slightly wider peak at lower energy with NiO at 854 eV after both AST, with a moderate increase in the intensity post OER-AST. Apparently, Ni rich alloy shows mainly $Ni(OH)_2$ on the surface whereas core-shell shows a surface covered with a mixture of NiO and $Ni(OH)_2$.

Pt-rich sample shows an interesting switch after OER/ORR AST as Ni signal is strongly increased in the form of $Ni(OH)_2$, whereas Pt signal displays a significant decrease especially post OER-AST. the drastic change may result from the formation of surface $Ni(OH)_2$.

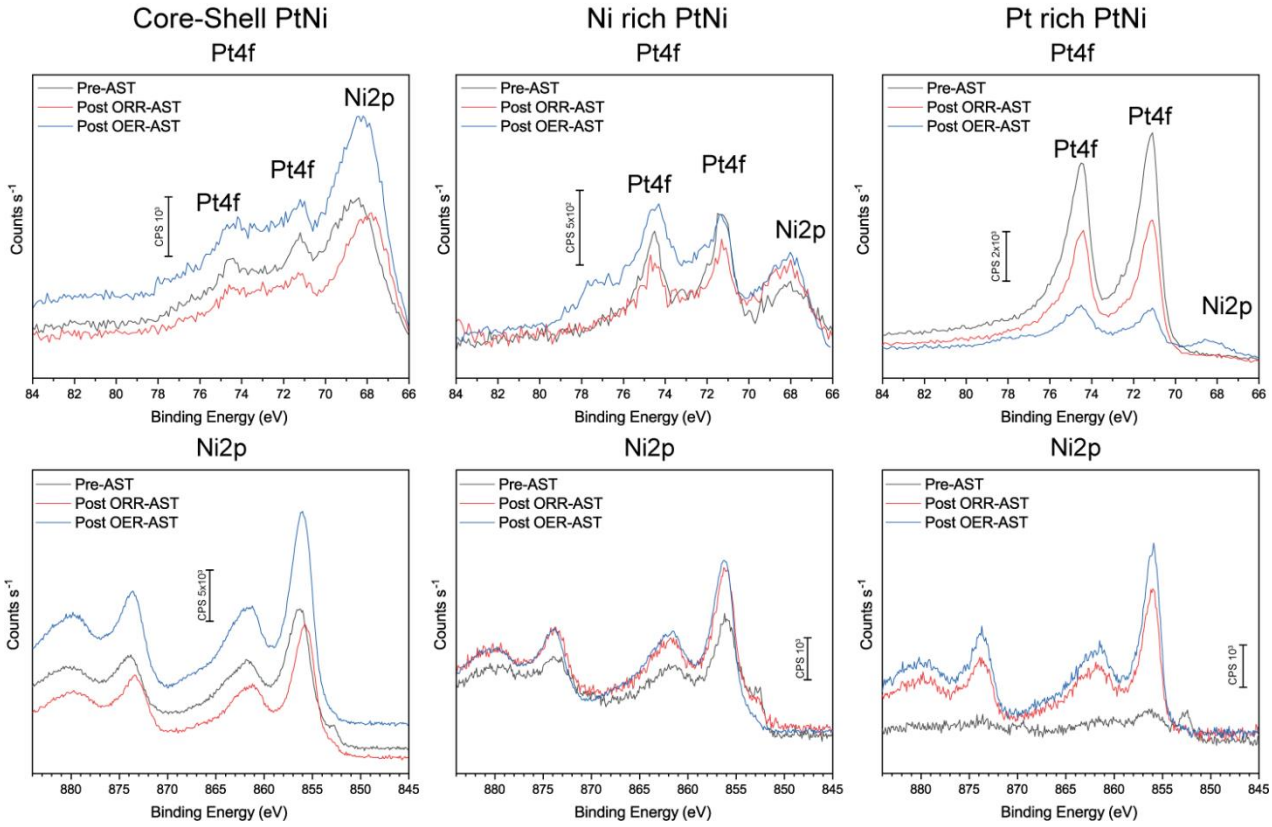

Figure 7. *XPS plots of Pt 4f and Ni 2p, pre and post AST of the PtNi samples.*

Figure 8 displays STEM-HAADF images, and EDS mapping of representative core-shell and Ni-rich NPS post OER-AST. These two samples were chosen since they display the largest OER activity. The core-shell structure partly remains after OER (Fig. 8a), the Ni shell has moderately worn off and diffused nearby while the Pt core is now partially exposed. This observation is consistent with the XPS which shows higher contents of both Pt and Ni. Ni-rich catalysts display the same octahedral morphology (Fig. 8b). The Pt skeleton is left barely untouched. Slight changes took place during the OER with the swelling of the Ni rich core, which now covers the Pt skeleton.

The post-OER STEM analysis confirms that the nanoparticles display a similar morphology after electrochemical cycling and validates the structure-properties relationship drawn in this article.

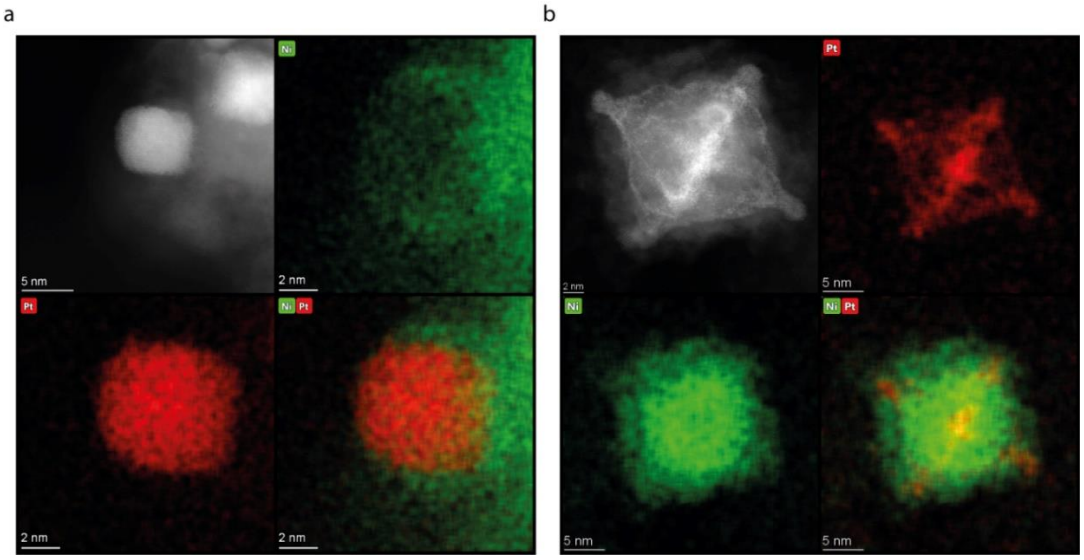

Figure 8. STEM-HAADF images and XEDS mapping of representative NPs; Core-Shell Pt@Ni (a), Ni-rich PtNi (b), after OER-AST,

The comparison between the catalysts reveals the important features of Pt-Ni ORR and OER electrocatalysts in alkaline electrolyte. Pt/C, a benchmark catalyst for ORR, displays a rapid and localized carbon degradation (nearby the Pt NPs) as a side catalytic reaction, which mostly results in the Pt NPs detachment: Pt catalyses formation of carbonate ions, which can lead to the growth of K_2CO_3 and promote the NPs detachment (see e.g. [27,29,53]). On the other end of the Pt-Ni phase diagram, Ni NPs displays a slight drift on the carbon support but do not detach from the carbon substrate. In the case of Ni rich alloys and core-shell NPs, the presence of Ni prevents Pt from catalysing the carbon corrosion and inhibits the formation of carbonates species and then K_2CO_3. Ni sites anchor the NPs onto the carbon support, significantly lower the detachment rate and extend the durability of the catalyst by removing one of the main origins for the particle losses. Moreover, the presence of both Pt and Ni/$Ni(OH)_2$ has a synergetic effect on the OER catalytic activity. Additionally, the OER post AST show no weakening of the activity for the core-shell samples compared to Ni/C, the activity of which slightly fades. This enhancement of catalytic activity and chemical stability is remarkable for OER, where most of the materials are prone to degradation.

Another important observation is the tendency of the metals to segregate in Ni rich NPs, mainly noticed by TEM measurements post-OER (Figure 8b) and XRD (Figure 6). Ni was driven to the surface and covered the particle surface, which mainly consists of $Ni(OH)_2$. The phase segregation is also observed on XRD with the shift of the peaks towards pure Pt and Ni phase.

4. Conclusions

Pt-rich alloy, Ni-rich alloy, and Pt@Ni were synthesized as mainly octahedral nanoparticles on carbon and the activity of the particles for ORR/OER in alkaline medium was measured after accelerated stress tests. The morphology and composition were evaluated by identical-location transmission electron microscopy (IL-TEM), X-ray photoelectron spectroscopy and X-ray diffraction before and after accelerated stress test. Compared to the monometallic Pt/C and Ni/C, the core-shell and Ni-rich alloy catalysts display high and stable OER activities, while the Pt-rich alloy was more suitable as ORR catalyst. All the combinations of PtNi demonstrate an improved attachment of the catalyst to the carbon support compared to Pt, confirming the crucial importance of Ni to stabilize the catalyst/carbon support tandem. In addition to the electrochemical stability, Ni-rich alloy and the Pt@Ni core-shell catalysts show high OER activity and durability upon accelerated stress test, as a result from a Ni-enrichment at the nanoparticles' surface. The synthesis of Pt core catalyst does not follow the intuitive ratio design of PGM catalyst which commonly aim at the presence of a Pt skin on the surface. More core-shell catalysts with a PGM core and an earth-abundant shell may share the same behavior with the Pt@Ni investigated herein.

ASSOCIATED CONTENT

Supporting Information.

XRF spectra of the Pt-Ni samples, PSD histograms of the PtNi NPs samples in their initial state, evolution of the electrochemical performances of Ni/C and Pt/C post OER-AST or ORR-AST, Ni^{2+}/Ni^{3+} redox electrochemical region pre and post ASTs, IL-TEM images of Ni/C and Pt/C pre and post both ASTs, percentage histograms of the lost particles post ASTs and shape change of the PtNi NPs samples, PSD comparison of the PtNi samples pre and post ASTs, XPS spectra of the O1s and C1s of the PtNi samples.

AUTHOR INFORMATION

Corresponding Authors
*E-mail: David.Zitoun@biu.ac.il

*E-mail: Marian.Chatenet@grenoble-inp.fr

NOTES

The authors declare no competing financial interest.

ACKNOWLEDGMENTS

This work was partially supported by the Planning & Budgeting Committee of the Council for Higher Education and the Prime Minister Office of Israel, in the framework of the INREP project and the

Centre of Excellence of Multifunctional Architectured Materials “CEMAM” n◦ ANR-10-LABX-44-01. The authors thank Samuel Hardisty for his help with the XPS analysis.

Reference

(1) Armstrong, R. C.; Wolfram, C.; De Jong, K. P.; Gross, R.; Lewis, N. S.; Boardman, B.; Ragauskas, A. J.; Ehrhardt-Martinez, K.; Crabtree, G.; Ramana, M. V. The Frontiers of Energy. *Nat. Energy* **2016**, *1* (1), 15020. https://doi.org/10.1038/nenergy.2015.20.

(2) Götz, M.; Lefebvre, J.; Mörs, F.; McDaniel Koch, A.; Graf, F.; Bajohr, S.; Reimert, R.; Kolb, T. Renewable Power-to-Gas: A Technological and Economic Review. *Renew. Energy* **2016**, *85*, 1371–1390. https://doi.org/10.1016/j.renene.2015.07.066.

(3) Jamesh, M. I.; Sun, X. Recent Progress on Earth Abundant Electrocatalysts for Oxygen Evolution Reaction (OER) in Alkaline Medium to Achieve Efficient Water Splitting – A Review. *J. Power Sources* **2018**, *400* (February), 31–68. https://doi.org/10.1016/j.jpowsour.2018.07.125.

(4) Shi, Q.; Zhu, C.; Du, D.; Lin, Y. Robust Noble Metal-Based Electrocatalysts for Oxygen Evolution Reaction. *Chem. Soc. Rev.* **2019**, *48* (12), 3181–3192. https://doi.org/10.1039/c8cs00671g.

(5) Roger, I.; Shipman, M. A.; Symes, M. D. Earth-Abundant Catalysts for Electrochemical and Photoelectrochemical Water Splitting. *Nat. Rev. Chem.* **2017**, *1*. https://doi.org/10.1038/s41570-016-0003.

(6) Zhang, B.; Zheng, X.; Voznyy, O.; Comin, R.; Bajdich, M.; García-Melchor, M.; Han, L.; Xu, J.; Liu, M.; Zheng, L.; De Arquer, F. P. G.; Dinh, C. T.; Fan, F.; Yuan, M.; Yassitepe, E.; Chen, N.; Regier, T.; Liu, P.; Li, Y.; De Luna, P.; Janmohamed, A.; Xin, H. L.; Yang, H.; Vojvodic, A.; Sargent, E. H. Homogeneously Dispersed Multimetal Oxygen-Evolving Catalysts. *Science (80-.).* **2016**, *352* (6283), 333–337. https://doi.org/10.1126/science.aaf1525.

(7) Zhang, X.; Zhao, Y.; Zhao, Y.; Shi, R.; Waterhouse, G. I. N.; Zhang, T. A Simple Synthetic Strategy toward Defect-Rich Porous Monolayer NiFe-Layered Double Hydroxide Nanosheets for Efficient Electrocatalytic Water Oxidation. *Adv. Energy Mater.* **2019**, *9* (24), 1–7. https://doi.org/10.1002/aenm.201900881.

(8) Li, J.; Zhou, Q.; Zhong, C.; Li, S.; Shen, Z.; Pu, J.; Liu, J.; Zhou, Y.; Zhang, H.; Ma, H. (Co/Fe)4O4 Cubane-Containing Nanorings Fabricated by Phosphorylating Cobalt Ferrite for Highly Efficient Oxygen Evolution Reaction. *ACS Catal.* **2019**, *9* (5), 3878–3887. https://doi.org/10.1021/acscatal.9b00293.

(9) Lai, J.; Huang, B.; Tang, Y.; Lin, F.; Zhou, P.; Chen, X.; Sun, Y.; Lv, F.; Guo, S. Barrier-Free Interface Electron Transfer on PtFe-Fe2C Janus-like Nanoparticles Boosts Oxygen Catalysis. *Chem* **2018**, *4* (5), 1153–1166. https://doi.org/10.1016/j.chempr.2018.02.010.

(10) Oezaslan, M.; Hasché, F.; Strasser, P. Oxygen Electroreduction on PtCo 3 , PtCo and Pt 3 Co Alloy Nanoparticles for Alkaline and Acidic PEM Fuel Cells . *J. Electrochem. Soc.* **2012**, *159* (4), B394–B405. https://doi.org/10.1149/2.075204jes.

(11) Gui, L.; Chen, Y.; He, B.; Li, G.; Xu, J.; Wang, Q.; Sun, W.; Zhao, L. Nickel-Based Bicarbonates as Bifunctional Catalysts for Oxygen Evolution and Reduction Reaction in Alkaline Media. *Chem.*

- *A Eur. J.* **2018**, *24* (67), 17665–17671. https://doi.org/10.1002/chem.201804118.

(12) Li, Y.; Li, Q.; Wang, H.; Zhang, L.; Wilkinson, D. P.; Zhang, J. Recent Progresses in Oxygen Reduction Reaction Electrocatalysts for Electrochemical Energy Applications. *Electrochem. Energy Rev.* **2019**, *2* (4), 518–538. https://doi.org/10.1007/s41918-019-00052-4.

(13) He, Q.; Cairns, E. J. Review - Recent Progress in Electrocatalysts for Oxygen Reduction Suitable for Alkaline Anion Exchange Membrane Fuel Cells. *J. Electrochem. Soc.* **2015**, *162* (14), F1504–F1539. https://doi.org/10.1149/2.0551514jes.

(14) Ge, X.; Sumboja, A.; Wuu, D.; An, T.; Li, B.; Goh, F. W. T.; Hor, T. S. A.; Zong, Y.; Liu, Z. Oxygen Reduction in Alkaline Media : From Mechanisms to Recent Advances of Catalysts. **2015**. https://doi.org/10.1021/acscatal.5b00524.

(15) Chang, F.; Yu, G.; Shan, S.; Skeete, Z.; Wu, J.; Luo, J.; Ren, Y.; Petkov, V.; Zhong, C. J. Platinum-Nickel Nanowire Catalysts with Composition-Tunable Alloying and Faceting for the Oxygen Reduction Reaction. *J. Mater. Chem. A* **2017**, *5* (24), 12557–12568. https://doi.org/10.1039/c7ta03266h.

(16) Oezaslan, M.; Hasché, F.; Strasser, P. PtCu 3, PtCu and Pt 3Cu Alloy Nanoparticle Electrocatalysts for Oxygen Reduction Reaction in Alkaline and Acidic Media. *J. Electrochem. Soc.* **2012**, *159* (4), 444–454. https://doi.org/10.1149/2.106204jes.

(17) Colón-Mercado, H. R.; Kim, H.; Popov, B. N. Durability Study of Pt3Ni1 Catalysts as Cathode in PEM Fuel Cells. *Electrochem. commun.* **2004**, *6* (8), 795–799. https://doi.org/10.1016/j.elecom.2004.05.028.

(18) Todoroki, N.; Takahashi, R.; Iijima, Y.; Yamada, Y.; Hayashi, T.; Wadayama, T. Platinum-Enriched Ni/Pt(111) Surfaces Prepared by Molecular Beam Epitaxy: Oxygen Reduction Reaction Activity and Stability. *Mater. Trans.* **2013**, *54* (9), 1735–1740. https://doi.org/10.2320/matertrans.M2013061.

(19) Chen, C.; Kang, Y.; Huo, Z.; Zhu, Z.; Huang, W.; Xin, H. L.; Snyder, J. D.; Li, D.; Herron, J. A.; Mavrikakis, M.; Chi, M.; More, K. L.; Li, Y.; Markovic, N. M.; Somorjai, G. A.; Yang, P.; Stamenkovic, V. R. Highly Crystalline Multimetallic Nanoframes with Three-Dimensional Electrocatalytic Surfaces. *Science (80-.).* **2014**, *343* (6177), 1339–1343. https://doi.org/10.1126/science.1249061.

(20) Becknell, N.; Son, Y.; Kim, D.; Li, D.; Yu, Y.; Niu, Z.; Lei, T.; Sneed, B. T.; More, K. L.; Markovic, N. M.; Stamenkovic, V. R.; Yang, P. Control of Architecture in Rhombic Dodecahedral Pt-Ni Nanoframe Electrocatalysts. *J. Am. Chem. Soc.* **2017**, *139* (34), 11678–11681. https://doi.org/10.1021/jacs.7b05584.

(21) Dubau, L.; Asset, T.; Chattot, R.; Bonnaud, C.; Vanpeene, V.; Nelayah, J.; Maillard, F. Tuning the Performance and the Stability of Porous Hollow PtNi/C Nanostructures for the Oxygen Reduction Reaction. *ACS Catal.* **2015**, *5* (9), 5333–5341. https://doi.org/10.1021/acscatal.5b01248.

(22) Yang, L. P.; Mi, J. L.; Liang, J. H.; Zu, Z. Y.; Zhang, P. Copper-Carbon: An Efficient Catalyst for Oxygen Reduction. *ACS Appl. Energy Mater.* **2019**, *2* (9), 6295–6301. https://doi.org/10.1021/acsaem.9b00867.

(23) Qian, Y.; Du, P.; Wu, P.; Cai, C.; Gervasio, D. F. Chemical Nature of Catalytic Active Sites for the Oxygen Reduction Reaction on Nitrogen-Doped Carbon-Supported Non-Noble Metal Catalysts. *J. Phys. Chem. C* **2016**, *120* (18), 9884–9896. https://doi.org/10.1021/acs.jpcc.6b02670.

(24) Cherevko, S.; Zeradjanin, A. R.; Keeley, G. P.; Mayrhofer, K. J. J. A Comparative Study on Gold and Platinum Dissolution in Acidic and Alkaline Media. *J. Electrochem. Soc.* **2014**, *161* (12), H822–H830. https://doi.org/10.1149/2.0881412jes.

(25) Cherevko, S.; Geiger, S.; Kasian, O.; Kulyk, N.; Grote, J. P.; Savan, A.; Shrestha, B. R.; Merzlikin, S.; Breitbach, B.; Ludwig, A.; Mayrhofer, K. J. J. Oxygen and Hydrogen Evolution Reactions on Ru, RuO2, Ir, and IrO2 Thin Film Electrodes in Acidic and Alkaline Electrolytes: A Comparative Study on Activity and Stability. *Catal. Today* **2016**, *262*, 170–180. https://doi.org/10.1016/j.cattod.2015.08.014.

(26) Schalenbach, M.; Kasian, O.; Ledendecker, M.; Speck, F. D.; Mingers, A. M.; Mayrhofer, K. J. J.; Cherevko, S. The Electrochemical Dissolution of Noble Metals in Alkaline Media. *Electrocatalysis* **2018**, *9* (2), 153–161. https://doi.org/10.1007/s12678-017-0438-y.

(27) Zadick, A.; Dubau, L.; Sergent, N.; Berthomé, G.; Chatenet, M. Huge Instability of Pt/C Catalysts in Alkaline Medium. *ACS Catal.* **2015**, *5* (8), 4819–4824. https://doi.org/10.1021/acscatal.5b01037.

(28) Lafforgue, C.; Zadick, A.; Dubau, L.; Maillard, F.; Chatenet, M. Selected Review of the Degradation of Pt and Pd-Based Carbon-Supported Electrocatalysts for Alkaline Fuel Cells : Towards Mechanisms of Degradation ~. **2018**, No. 3, 229–238. https://doi.org/10.1002/fuce.201700094.

(29) Lafforgue, C.; Maillard, F.; Martin, V.; Dubau, L.; Chatenet, M. Degradation of Carbon-Supported Platinum-Group-Metal Electrocatalysts in Alkaline Media Studied by in Situ Fourier Transform Infrared Spectroscopy and Identical-Location Transmission Electron Microscopy. *ACS Catal.* **2019**, 5613–5622. https://doi.org/10.1021/acscatal.9b00439.

(30) Chatenet, M.; Dubau, L.; Dekel, D. R. Accelerated Stress Test of Pt / C Nanoparticles in an Interface with an Anion-Exchange Membrane An Identical-Location Transmission Electron Microscopy Study Cle M. **2018**. https://doi.org/10.1021/acscatal.7b04055.

(31) Zadick, A.; Dubau, L.; Demirci, U. B.; Chatenet, M. Effects of Pd Nanoparticle Size and Solution Reducer Strength on Pd/C Electrocatalyst Stability in Alkaline Electrolyte. *J. Electrochem. Soc.* **2016**, *163* (8), F781–F787. https://doi.org/10.1149/2.0141608jes.

(32) Zadick, A.; Dubau, L.; Zalineeva, A.; Coutanceau, C.; Chatenet, M. Electrochemistry Communications When Cubic Nanoparticles Get Spherical : An Identical Location Transmission Electron Microscopy Case Study with Pd in Alkaline Media. *Electrochem. commun.* **2014**, *48*, 1–4. https://doi.org/10.1016/j.elecom.2014.07.020.

(33) Cui, C.; Gan, L.; Heggen, M.; Rudi, S.; Strasser, P. Compositional Segregation in Shaped Pt Alloy Nanoparticles and Their Structural Behaviour during Electrocatalysis. *Nat. Mater.* **2013**, *12* (8), 765–771. https://doi.org/10.1038/nmat3668.

(34) Vij, V.; Sultan, S.; Harzandi, A. M.; Meena, A.; Tiwari, J. N.; Lee, W. G.; Yoon, T.; Kim, K. S. Nickel-Based Electrocatalysts for Energy-Related Applications: Oxygen Reduction, Oxygen Evolution, and Hydrogen Evolution Reactions. *ACS Catal.* **2017**, *7* (10), 7196–7225. https://doi.org/10.1021/acscatal.7b01800.

(35) She, Z. W.; Kibsgaard, J.; Dickens, C. F.; Chorkendorff, I.; Nørskov, J. K.; Jaramillo, T. F. Combining Theory and Experiment in Electrocatalysis: Insights into Materials Design. *Science (80-.).* **2017**, *355* (6321). https://doi.org/10.1126/science.aad4998.

(36) Garsany, Y.; Singer, I. L.; Swider-Lyons, K. E. Impact of Film Drying Procedures on RDE Characterization of Pt/VC Electrocatalysts. *J. Electroanal. Chem.* **2011**, *662* (2), 396–406.

https://doi.org/10.1016/j.jelechem.2011.09.016.

(37) Mayrhofer, K. J. J.; Crampton, A. S.; Wiberg, G. K. H.; Arenz, M. Analysis of the Impact of Individual Glass Constituents on Electrocatalysis on Pt Electrodes in Alkaline Solution. *J. Electrochem. Soc.* **2008**, *155* (6), P78. https://doi.org/10.1149/1.2904882.

(38) Mayrhofer, K. J. J.; Wiberg, G. K. H.; Arenz, M. Impact of Glass Corrosion on the Electrocatalysis on Pt Electrodes in Alkaline Electrolyte. *J. Electrochem. Soc.* **2008**, *155* (1), P1. https://doi.org/10.1149/1.2800752.

(39) Mayrhofer, K. J. J.; Ashton, S. J.; Meier, J. C.; Wiberg, G. K. H.; Hanzlik, M.; Arenz, M. Non-Destructive Transmission Electron Microscopy Study of Catalyst Degradation under Electrochemical Treatment. *J. Power Sources* **2008**, *185* (2), 734–739. https://doi.org/10.1016/j.jpowsour.2008.08.003.

(40) Shviro, M.; Gocyla, M.; Polani, S.; Heggen, M.; Zitoun, D.; Dunin-Borkowski, R. E. Morphological, Structural, and Compositional Evolution of Pt–Ni Octahedral Electrocatalysts with Pt-Rich Edges and Ni-Rich Core: Toward the Rational Design of Electrocatalysts for the Oxygen Reduction Reaction. *Part. Part. Syst. Charact.* **2019**, *36* (3), 1–6. https://doi.org/10.1002/ppsc.201800442.

(41) Shviro, M.; Zitoun, D. Nickel Nanocrystals: Fast Synthesis of Cubes, Pyramids and Tetrapods. *RSC Adv.* **2013**, *3* (5), 1380–1387. https://doi.org/10.1039/c2ra22024e.

(42) Conway, B. E.; Jerkiewicz, G. Surface Orientation Dependence of Oxide Film Growth at Platinum Single Crystals. *J. Electroanal. Chem.* **1992**, *339* (1–2), 123–146. https://doi.org/10.1016/0022-0728(92)80448-D.

(43) Hammer, B.; Nørskov, J. K. Electronic Factors Determining the Reactivity of Metal Surfaces. *Surf. Sci.* **1995**, *343* (3), 211–220. https://doi.org/10.1016/0039-6028(96)80007-0.

(44) Huang, X.; Cao, L.; Chen, Y.; Zhu, E.; Lin, Z.; Li, M.; Yan, A.; Zettl, A.; Wang, Y. M.; Duan, X.; Mueller, T. High-Performance Transition Metal – Doped Pt 3 Ni Octahedra for Oxygen Reduction ReactionHuang, X., Cao, L., Chen, Y., Zhu, E., Lin, Z., Li, M., … Mueller, T. (2015). High-Performance Transition Metal – Doped Pt 3 Ni Octahedra for Oxygen Reduction Reactio. *Science (80-.).* **2015**, *348* (6240), 1230–1234.

(45) Stamenković, V.; Schmidt, T. J.; Ross, P. N.; Marković, N. M. Surface Segregation Effects in Electrocatalysis: Kinetics of Oxygen Reduction Reaction on Polycrystalline Pt3Ni Alloy Surfaces. *J. Electroanal. Chem.* **2003**, *554–555* (1), 191–199. https://doi.org/10.1016/S0022-0728(03)00177-3.

(46) Hall, D. E. Electrodes for Alkaline Water Electrolysis. *J. Electrochem. Soc.* **1981**, *128* (4), 740. https://doi.org/10.1149/1.2127498.

(47) Kovac, Z.; Markovich, V.; Romankiw, L. T.; West, K. W.; West, K. W.; Journal, T.; Meek, R. L.; Poskanzer, A. M.; Zuman, P.; Engineering, E.; Tobias, C.; Journal, T.; Gottesfeld, S.; Laser, D.; Takematsu, H.; Nihei, K.; Journal, T.; Nagasaka, H.; Goto, F.; Weiner, J. A.; Schnable, G. L.; Weiner, J. A.; Amico, J. F. D.; West, K. W.; West, K. W.; Horkans, J.; Cahan, B. D.; Yeager, E.; Romankiw, L. T.; Kohra, K. Ni (OH) 2-1mpregnated Anodes for Alkaline Water Electrolysis. *J. Electroanal. Chem.* **1983**, *130* (2), 317–321.

(48) Darling, R. M.; Meyers, J. P. Kinetic Model of Platinum Dissolution in PEMFCs. *J. Electrochem. Soc.* **2003**, *150* (11), A1523. https://doi.org/10.1149/1.1613669.

(49) Castanheira, L.; Dubau, L.; Mermoux, M.; Berthomé, G.; Caqué, N.; Rossinot, E.; Chatenet, M.; Maillard, F. Carbon Corrosion in Proton-Exchange Membrane Fuel Cells: From Model

Experiments to Real-Life Operation in Membrane Electrode Assemblies. *ACS Catal.* **2014**, *4* (7), 2258–2267. https://doi.org/10.1021/cs500449q.

(50) Castanheira, L.; Silva, W. O.; Lima, F. H. B.; Crisci, A.; Dubau, L.; Maillard, F. Carbon Corrosion in Proton-Exchange Membrane Fuel Cells: Effect of the Carbon Structure, the Degradation Protocol, and the Gas Atmosphere. *ACS Catal.* **2015**, *5* (4), 2184–2194. https://doi.org/10.1021/cs501973j.

(51) Ferreira, P. J.; la O', G. J.; Shao-Horn, Y.; Morgan, D.; Makharia, R.; Kocha, S.; Gasteiger, H. A. Instability of Pt/C Electrocatalysts in Proton Exchange Membrane Fuel Cells. *J. Electrochem. Soc.* **2005**, *152* (11), A2256. https://doi.org/10.1149/1.2050347.

(52) Yasuda, K.; Taniguchi, A.; Akita, T.; Ioroi, T.; Siroma, Z. Platinum Dissolution and Deposition in the Polymer Electrolyte Membrane of a PEM Fuel Cell as Studied by Potential Cycling. *Phys. Chem. Chem. Phys.* **2006**, *8* (6), 746–752. https://doi.org/10.1039/b514342j.

(53) Lafforgue, C.; Zadick, A.; Dubau, L.; Maillard, F.; Chatenet, M. Selected Review of the Degradation of Pt and Pd-Based Carbon-Supported Electrocatalysts for Alkaline Fuel Cells: Towards Mechanisms of Degradation. *Fuel Cells* **2018**, *18* (3), 229–238. https://doi.org/10.1002/fuce.201700094.

(54) Zadick, A.; Dubau, L.; Artyushkova, K.; Serov, A.; Atanassov, P.; Chatenet, M. Nickel-Based Electrocatalysts for Ammonia Borane Oxidation: Enabling Materials for Carbon-Free-Fuel Direct Liquid Alkaline Fuel Cell Technology. *Nano Energy* **2017**, *37* (May), 248–259. https://doi.org/10.1016/j.nanoen.2017.05.035.

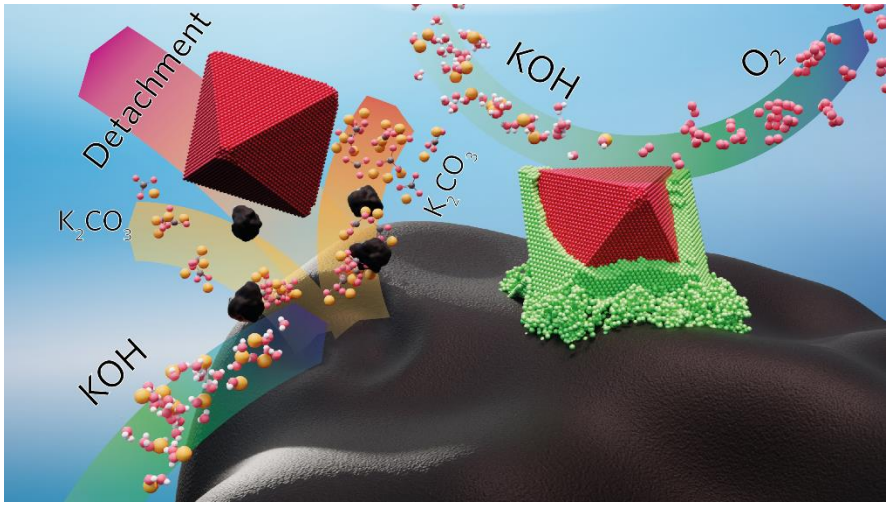

Graphical abstract: Pt detachment from the carbon support vs. Pt@Ni stability during the oxygen evolution reaction